Uncertainties in Deep Inelastic Scattering for GeV-Scale Neutrinos Experiments

D. Xu [1, *]

[1] *Physics Department, Columbia University, New York, NY 10027, USA*

(Dated: December 17, 2024)

The cross-sections for deep inelastic scattering (DIS) of leptons on nuclei are calculated, with a focus on their systematic uncertainties and implications for $\mathcal{O}$(GeV) neutrino oscillation experiments. The calculation begins with quark-electron scattering via electromagnetic interactions and extends to neutrino-quark interactions. Using the quark-parton model, the structure functions governing these interactions are derived. The analysis highlights differences in cross-sections between charged and neutral leptons, illustrating the complexities of weak interactions. Approximations are discussed, emphasizing their validity at high momentum transfers, consistent with the asymptotic freedom of quantum chromodynamics. The persistence of large systematic uncertainties underscores the need for direct experimental measurements of DIS cross-sections and supports the critical role of the near-far detector configuration in the DUNE experiment.

I. INTRODUCTION

Neutrinos, the lightest leptons described in the Standard Model (SM), have long been considered exotic particles. Since the first experimental confirmation of their existence [1], neutrinos have attracted significant interest due to their unique properties. The accidental observation of a neutrino burst from a supernova opened the door to neutrino astronomy [2]. The solar neutrino problem [3] and other observed anomalies suggested that neutrinos might have different masses and could oscillate between phases. Following the firm verification of neutrino oscillations by solar, atmospheric, and reactor neutrino experiments—including the Sudbury Neutrino Observatory (SNO)[4], Super-Kamiokande (SK) [5], and KamLAND [6]—the measurement of oscillation parameters has become the primary goal of many neutrino experiments, such as T2K [7], Daya Bay [8], and NOνA [9].

Accurate measurements of neutrino properties depend on a precise description of neutrino interactions and the detector's response to the resulting final-state particles. A comprehensive overview of neutrino interactions is provided in [10]. Depending on the neutrino energy E_ν and the target isotopes, different interaction regimes are relevant. For example, MeV-scale neutrinos from the Sun and reactors are typically detected via inverse beta decay [11] through charged-current (CC) reactions and elastic scattering (ES) through neutral currents in various detector materials. At sub-GeV and $\mathcal{O}$(1)GeV energies, especially among accelerator neutrinos, CC quasielastic scattering (e.g., $\bar{\nu}_\mu p \to \mu^+ n$) and resonance scattering processes (e.g., $\bar{\nu}_\mu n \to \mu^+ \Lambda^- \to \mu^+ n\pi^-$) become the leading contributions. Starting at $\mathcal{O}$(10)GeV, above the resonance region, inelastic scattering dominates with a final-state invariant mass $W \geq 2$GeV (e.g., $\bar{\nu}_\mu p \to \mu^+ X$).

Beyond the relatively straightforward lepton-lepton interactions, calculating lepton-nucleus interactions requires understanding the interactions within nucleons (and the nucleus), which involve quantum chromodynamics (QCD). Due to the complexity of QCD and the presence of dynamically generated gluons, perturbative methods become impractical at certain energies. Although there is no established boundary between shallow inelastic scattering (SIS) and deep inelastic scattering (DIS), as illustrated in Fig. 5, the threshold of momentum transfer Q^2 is usually considered to be a few GeV^2, which also separates the non-perturbative and perturbative regions.

In calculating the cross-section of lepton-nucleus inelastic scattering, the quark-parton model is typically applied, where the cross-section is approximately the sum of the neutrino's interactions with individual quarks, with special consideration given to quark distributions within nucleons, known as parton distribution functions (PDFs). These PDFs are crucial inputs for structure functions, which directly enter the cross-section calculations. While the model suffices for rough calculations at high Q^2, applying the results to practical neutrino experiments requires complex phenomenological parameterizations and careful consideration of originating uncertainties. Although theoretical predictions of PDFs are still evolving, experimental data provide these functions for use in calculations and predictions.

This paper focuses on the formulation of DIS cross-section calculations and the impact of their uncertainties on future neutrino experiments. It first provides a brief overview of the DIS formulation, progressing from lepton-quark interactions and elastic electron-proton interactions to DIS calculations. Experimental data from HERA [12, 13] will be used to illustrate the complexity of the determination of the structure function. In the cross-section calculations for the final part of the paper, well-accepted (Bodek-Yang [14]) and recently developed (NNSFν [15]) models will be compared to illustrate potential theoretical systematic uncertainties in neutrino experiments. Finally, a toy experiment with liquid argon (LAr), similar to the DUNE [16] experiment, is established to evaluate the impact of these uncertainties on the sensitivity to targeted oscillation parameters, such as θ_{23} and δ_{cp}.

* dacheng.xu@columbia.edu

II. LEPTON-NUCLEUS ELASTIC SCATTERING

In this section, the elastic electron-proton scattering and neutrino–quark scattering are demonstrated for preparation and comparison with the inelastic scattering. The $V-A$ structure of weak interaction in neutrino-quark scattering is discussed and will work as an argument in the simplification of the neutrino oscillation experiment in Sec. V.

A. Electron-proton elastic scattering

Protons are charged, and electromagnetic (EM) interaction is stronger than weak interaction. For an electron with low enough energy, the momentum transfer between it and a static proton is elastic because the final state still includes the electron and proton.

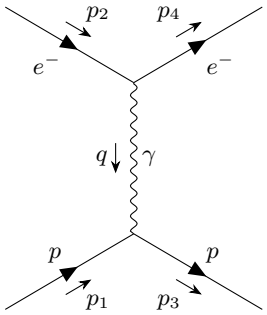

FIG. 1. The Feynman diagram of electron-proton elastic scattering, where the proton is seen as a point-like particle.

Fig. 1 shows the EM scattering process between an electron and proton while the momentum transfer q is low enough so the proton is seen as a point-like particle. Define the scattering angle θ of the electron as the angle between the direction after and before the scattering. For the general case, the four-momenta of the initial- and final-state particles can be defined as

$$p_1 = (E_1, 0, 0, E_1) \tag{1}$$
$$p_2 = (m_p, 0, 0, 0) \tag{2}$$
$$p_3 = (E_3, 0, E_3 \sin\theta, E_3 \cos\theta) \tag{3}$$
$$p_4 = (E_4, \mathbf{p}_4). \tag{4}$$

Assuming the electron energy is sufficiently large that the mass of the electron can be neglected, the matrix element for the elastic scattering process $e^- p \to e^- p$ is given by

$$\begin{aligned}\langle|\mathcal{M}_{fi}|^2\rangle =& \frac{8e^4}{(p_1-p_3)^4}\left[(p_1\cdot p_2)(p_3\cdot p_4)\right.\\ &\left.+(p_1\cdot p_4)(p_2\cdot p_3) - m_p^2(p_1\cdot p_3)\right]\end{aligned} \tag{5}$$

The four-momentum squared of the virtual photon, $q^2 = (p_1 - p_3)^2$, also can be expressed in terms of E_3 and θ using

$$\begin{aligned}q^2 &= (p_1-p_3)^2 = p_1^2 + p_3^2 - 2p_1\cdot p_3\\ &\approx -2E_1E_3(1-\cos\theta),\end{aligned} \tag{6}$$

where the terms $p_1 \cdot p_1 = p_3 \cdot p_3 = m_e^2$ have been neglected. To a good approximation,

$$Q^2 \equiv q^2 = -4E_1E_3\sin^2\frac{\theta}{2}, \tag{7}$$

where Q^2 is defined to make the variable positive. After applying the four-momentum to $\langle|\mathcal{M}_{fi}|^2\rangle$, the spin-averaged matrix element squared is expressed as

$$\langle|\mathcal{M}_{fi}|^2\rangle = \frac{m_p^2e^4}{E_1E_3\sin^4(\theta/2)}\left[\cos^2\frac{\theta}{2} + \frac{Q^2}{2m_p^2}\sin^2\frac{\theta}{2}\right]. \tag{8}$$

The differential cross-section can be obtained as

$$\frac{\mathrm{d}\sigma}{\mathrm{d}\Omega} \approx \frac{1}{64\pi^2}\left(\frac{E^3}{m_pE_1}\right)^2\langle|\mathcal{M}_{fi}|^2\rangle. \tag{9}$$

So the differential cross section for the scattering of relativistic electrons from a proton that is initially at rest is

$$\frac{\mathrm{d}\sigma}{\mathrm{d}\Omega} = \frac{\alpha^2}{4E_1^2\sin^4(\theta/2)}\frac{E_3}{E_1}\left(\cos^2\frac{\theta}{2} + \frac{Q^2}{2m_p^2}\sin^2\frac{\theta}{2}\right). \tag{10}$$

It is important to note that although the differential cross-section is expressed in terms of Q^2, E_3, θ, there is only one independent variable: both Q^2, E_3 can be expressed in terms of the scattering angle of the electron. This is also true when expressing the cross-section of DIS.

$$E_3 = \frac{E_1m_p}{m_p + E_1(1-\cos\theta)} \tag{11}$$
$$Q^2 = \frac{2m_pE_1^2(1-\cos\theta)}{m_p + E_1(1-\cos\theta)} \tag{12}$$

Therefore, if the scattering angle of the electron is measured in the elastic scattering process, the entire kinematics of the interaction is determined. Furthermore, because the energy of an elastically scattered electron at a particular angle must be equal to E_3 given above, by measuring the energy and angle of the scattered electron, it is possible to confirm that the interaction was indeed elastic and that the unobserved proton remained intact.

As electron energy grows, the inner structure of the proton is visible because the wavelength of an electron is small enough to interact with the substructure of the proton.

The charge density inside the proton can be expressed as $C\rho(\mathbf{r}')$, where C is the total charge and $\rho(\mathbf{r}')$ is the charge distribution normalized to unity

$$\int \rho(\mathbf{r}')\,\mathrm{d}^3\mathrm{r}' = 1. \tag{13}$$

The potential at a distance $\mathbf{r}$ from the origin, written in terms of charge density, is simply

$$V(\mathbf{r}) = \int \frac{C\rho(\mathbf{r}')}{4\pi|\mathbf{r}-\mathbf{r}'|}\,\mathrm{d}^3\mathrm{r}'. \tag{14}$$

Using Born approximation, where the wavefunctions of the initial state and scattered electrons are expressed as the plane waves, $\psi_i = e^{i(\mathbf{p}_1\cdot\mathbf{r}-Et)}$ and $\psi_f = e^{i(\mathbf{p}_3\cdot\mathbf{r}-Et)}$, the lowest-order matrix element for the scattering process is

$$\mathcal{M}_{fi} = \langle\psi_f|V(\mathbf{r})|\psi_i\rangle = \int e^{-i\mathbf{p}_3\cdot\mathbf{r}}V(\mathbf{r})e^{i\mathbf{p}_1\cdot\mathbf{r}}\,\mathrm{d}^3\mathrm{r}. \tag{15}$$

Writing $\mathbf{q} = \mathbf{p}_1 - \mathbf{p}_3$ and using the potential calculated in Eq. 14 leads to

$$\mathcal{M}_{fi} = \iint e^{i\mathbf{q}\cdot\mathbf{r}}\frac{C\rho(\mathbf{r}')}{4\pi|\mathbf{r}-\mathbf{r}'|}\,\mathrm{d}^3\mathbf{r}'\,\mathrm{d}^3\mathbf{r} \tag{16}$$

$$= \iint e^{i\mathbf{q}\cdot(\mathbf{r}-\mathbf{r}')}e^{i\mathbf{q}\cdot\mathbf{r}'}\frac{C\rho(\mathbf{r}')}{4\pi|\mathbf{r}-\mathbf{r}'|}\,\mathrm{d}^3\mathbf{r}'\,\mathrm{d}^3\mathbf{r} \tag{17}$$

$$= \int e^{i\mathbf{q}\cdot\mathbf{R}}\frac{C}{4\pi|\mathbf{R}|}\int \rho(\mathbf{r}')e^{i\mathbf{q}\cdot\mathbf{r}'}\,\mathrm{d}^3\mathbf{r}'. \tag{18}$$

So when considering the charge distribution inside the proton, essentially a form factor $F(\mathbf{q}^2)$ is the needed additional factor in the matrix element. $F(\mathbf{q}^2)$ is given by

$$F(\mathbf{q}^2) = \int \rho(\mathbf{r})e^{i\mathbf{q}\cdot\mathbf{r}}\,\mathrm{d}^3(\mathbf{r}). \tag{19}$$

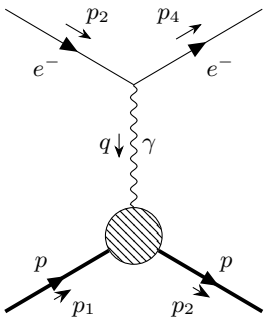

FIG. 2. The Feynman diagram of electron-proton elastic scattering, while the proton has a finite size.

Fig. 2 shows the process of elastic scattering, considering the finite size and distribution inside the proton. But for practical usage of the form factors, the finite size of a proton in elastic scattering is accounted for by two form factors, one related to the charge distribution of the proton, $G_E(Q^2)$, and the other related to the magnetic momentum distribution within the proton, $G_M(Q^2)$. It can be shown that the most general Lorenz-invariant form for electron-proton scattering via the exchange of a single photon, known as *Rosenbluth formula*, is

$$\frac{\mathrm{d}\sigma}{\mathrm{d}\Omega} = \frac{\alpha^2}{4E_1^2\sin^4(\theta/2)}\frac{E_3}{E_1}\left(\frac{G_E^2+\tau G_M^2}{(1+\tau)}\cos^2\frac{\theta}{2} + 2\tau G_M^2\sin^2\frac{\theta}{2}\right), \tag{20}$$

where τ is given by

$$\tau = \frac{Q^2}{4m_p^2}. \tag{21}$$

In the Lorentz-invariant Rosenbluth formula, the form factors $G_E(Q^2)$ and $G_M(Q^2)$ are functions of the four-momentum squared of the virtual photon, but they can not be interpreted simply as the Fourier transforms of the charge and magnetic moment distributions of the proton because of Eq. 6. The Q^2 and $\mathbf{q}^2$ coincides only when $Q^2 \ll m_p^2$ (low-Q^2 limit). In the low-Q^2 limit, the two factors are expressed as

$$G_E(Q^2) \approx G_E(\mathbf{q}^2) = \int e^{i\mathbf{q}\cdot\mathbf{r}}\rho(\mathbf{r})\,\mathrm{d}^3(\mathbf{r}) \tag{22}$$

$$G_M(Q^2) \approx G_M(\mathbf{q}^2) = \int e^{i\mathbf{q}\cdot\mathbf{r}}\mu(\mathbf{r})\,\mathrm{d}^3(\mathbf{r}). \tag{23}$$

B. Neutrino-quark and antineutrino-quark scattering

In this section, the (anti-)neutrino-quark scattering is discussed. When discussing neutrino scatterings, some approximations can be easily applied to simplify the calculation.

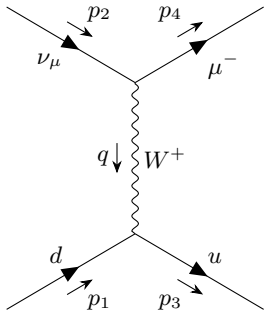

FIG. 3. The Feynman diagram of neutrino-quark scattering.

Fig. 3 shows a typical neutrino-quark scattering. Because the quark is known to not have a substructure, this

scattering is naturally elastic. The highest-energy neutrinos produced in an accelerator-based neutrino beam had $E_\nu = 400$ GeV, for which $Q^2 \leq 750$ GeV^2. This momentum transfer is sufficiently small that, for all practical purposes, the weak interaction propagator can be approximated by

$$\frac{-ig_{\mu\nu}}{q^2 - m_W^2} \to \frac{ig_{\mu\nu}}{m_W^2}. \tag{24}$$

So, neglecting the q^2 dependence of the propagator, the matrix element for the Feynman diagram can be expressed as

$$\begin{aligned}\mathcal{M}_{fi} =& \frac{g_W^2}{2m_W^2} g_{\mu\nu} \left[\bar{u}(p_3)\gamma^\mu \frac{1}{2}(1-\gamma^5)u(p_1)\right] \\ &\cdot \left[\bar{u}(p_4)\gamma^\nu \frac{1}{2}(1-\gamma^5)u(p_2)\right].\end{aligned} \tag{25}$$

For high-energy neutrino scattering, both the masses of the neutrinos and quarks are sufficiently small that the left-hand (LH) chiral states are effectively identical to the LH helicity state, so Eq. 25 can be written as

$$\mathcal{M}_{fi} = \frac{g_W^2}{2m_W^2} g_{\mu\nu} \left[\bar{u}_\downarrow(p_3)\gamma^\mu u_\downarrow(p_1)\right] \left[\bar{u}_\downarrow(p_4)\gamma^\nu u_\downarrow(p_2)\right] \tag{26}$$

$$= \frac{g_W^2}{2m_W^2} j_\ell \cdot j_q, \tag{27}$$

where $j_\ell = \bar{u}_\downarrow(p_3)\gamma^\mu u_\downarrow(p_1)$ and $j_q = \bar{u}_\downarrow(p_4)\gamma^\nu u_\downarrow(p_2)$ are respectively the lepton and quark currents. Evaluating the matrix elements in the center-of-mass frame. Using the same definition of scattering angle in the process described by Fig. 1, the matrix element for $\nu_\mu d \to \mu^- u$ can be evaluated as

$$\mathcal{M}_{\nu q} = \frac{g_W^2}{m_W^2}\hat{s}, \tag{28}$$

where $\hat{s} = (2E)^2$ is the $\nu_\mu d$ center-of-mass energy. The interaction occurs in the $S_z = 0$ state because both the quark and neutrino are left-handed. In the limit where the particle masses can be neglected, the center-of-mass frame differential cross-section is

$$\frac{\mathrm{d}\sigma}{\mathrm{d}\Omega} = \frac{1}{64\pi^2\hat{s}} \langle |\mathcal{M}_{fi}|^2 \rangle = \left(\frac{g_W^2}{8\sqrt{2}\pi m_W^2}\right)\hat{s}. \tag{29}$$

Using $G_F = (\sqrt{2}g_W^2)/(8m_W^2)$, the differential cross-section can be written as

$$\frac{\mathrm{d}\sigma_{\nu q}}{\mathrm{d}\Omega} = \frac{G_F^2}{4\pi^2}\hat{s}. \tag{30}$$

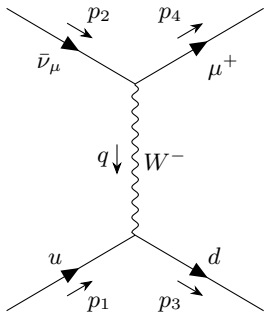

FIG. 4. The Feynman diagram of antineutrino-quark scattering.

But for neutrino-quark interaction, shown in Fig. 4, the cross-section has to be modified considering the $V-A$ structure, and there is only right-hand (RH) antineutrino, while neutrino mass is assumed to be zero in the $\mathcal{O}$(GeV) neutrino interactions.

While writing the matrix element again

$$\begin{aligned}\mathcal{M}_{fi} =& \frac{g_W^2}{2m_W^2} g_{\mu\nu} \left[\bar{v}(p_1)\gamma^\mu \frac{1}{2}(1-\gamma^5)u(p_3)\right] \\ &\cdot \left[\bar{u}(p_4)\gamma^\nu \frac{1}{2}(1-\gamma^5)u(p_2)\right],\end{aligned} \tag{31}$$

it can be simplified as

$$\mathcal{M}_{fi} = \frac{g_W^2}{2m_W^2} g_{\mu\nu} \left[\bar{v}_\uparrow(p_1)\gamma^\mu u_\uparrow(p_3)\right] \left[\bar{u}_\downarrow(p_4)\gamma^\nu u_\downarrow(p_2)\right]. \tag{32}$$

The spinors are listed as

$$\begin{aligned}\bar{v}_\uparrow(p_1) &= \sqrt{E}\begin{pmatrix}0\\-1\\0\\1\end{pmatrix}; \quad u_\uparrow(p_3) = \sqrt{E}\begin{pmatrix}\cos\theta\\\sin\theta\\\cos\theta\\\sin\theta\end{pmatrix} \\ \bar{u}_\downarrow(p_4) &= \sqrt{E}\begin{pmatrix}-\cos\theta\\-\sin\theta\\\cos\theta\\\sin\theta\end{pmatrix}; \quad u_\downarrow(p_2) = \sqrt{E}\begin{pmatrix}0\\1\\0\\-1\end{pmatrix}.\end{aligned} \tag{33}$$

Plugin-in them into Eq. 32,

$$\mathcal{M}_{\bar{\nu}q} = \frac{1}{2}\cos\theta \frac{g_W^2}{m_W^2}\hat{s} \tag{34}$$

$$\frac{\mathrm{d}\sigma_{\bar{\nu}q}}{\mathrm{d}\Omega} = \frac{G_F^2}{16\pi^2}(1+\cos\theta)^2\hat{s}. \tag{35}$$

Averaging the scattering angle, we got a relation of the cross-section of neutrino-quark scattering with the same neutrino energy

$$\frac{\sigma_{\bar{\nu}q}}{\sigma_{\nu q}} = \frac{1}{3}. \tag{36}$$

So later in Sec. V the approximation of only neutrino-nucleus DIS happens for $\mathcal{O}$(GeV) (anti-)neutrino is made given the assumed neutrino and antineutrino flux is similar. More details will be discussed in that section.

III. LEPTON-NUCLEUS INELASTIC SCATTERING

The inelastic scattering considers the rest mass change of the final state particles. The incident energy of leptons is absorbed and stored (temporarily but longer than the interaction happens) in the final state of hadron(s).

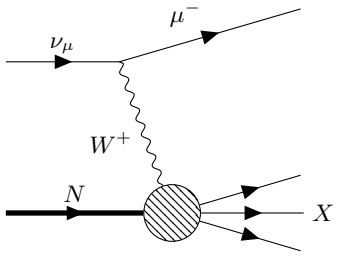

FIG. 5. Typical DIS of ν_μ. The final state X is not the initial nucleus N.

As a typical inelastic scattering shown in Fig. 5, the final state X is not a proton. The rest mass square of the final state is defined as $W^2 = p_4^2$ to aid the calculation of kinematic variables. Besides Q^2 defined in Sec. II A, the *Bjorken* x and y are defined to describe how inelastic the process is. The Lorentz-invariant dimensionless quantity Bjorken x is defined as

$$x \equiv \frac{Q^2}{2p_2 \cdot q}. \tag{37}$$

It is also called the "elasticity". While W^2 is related to Q^2 as

$$W^2 \equiv p_4^2 = (q + p_2)^2 = q^2 + 2p_2 \cdot q + p^2 \tag{38}$$

$$W^2 + Q^2 - m_p^2 = 2p \cdot q, \tag{39}$$

x can be alternatively expressed as

$$x = \frac{Q^2}{Q^2 + W^2 - m_p^2}. \tag{40}$$

Because $Q^2 \geq 0$ and $W^2 \geq m_p^2$, $0 \leq x \leq 1$. When x is closer to 0 (1), the interaction is more inelastic (elastic). When W^2 increases, the x decreases, showing more energy transfer and is stored in the final hadron states. So x is regarding the change in final state hadron.

Another dimensionless Lorentz-invariant quantity y, also known as "inelasticity" is defined as

$$y \equiv \frac{p_2 \cdot q}{p_2 \cdot p_1}. \tag{41}$$

It can be easily proven that in the proton-at-rest frame, this variable is

$$y = \frac{m_p(E_1 - E_3)}{m_p E_1} = 1 - \frac{E_3}{E_1}. \tag{42}$$

Because y is Lorentz invariant, this expression is also valid in other frames. The y is essentially the fractional energy loss of the incident neutrino. Naturally, $0 \leq y \leq 1$, so y is regarding the final state of (anti-)lepton.

For a fixed center-of-mass frame energy,

$$s = (p_1 + p_2)^2 = p_1^2 + p^2 + 2p_1 p_2 = 2p_1 p_2 + m_p^2 + m_\mu^2. \tag{43}$$

Since the lepton mass m_μ is much smaller than m_p^2, to a good approximation

$$2p_1 \cdot p_2 \approx s - m_p^2. \tag{44}$$

Combine these approximations and relations, a relation between Q^2, s, x, and y can be shown

$$Q^2 = (s - m_p^2)xy. \tag{45}$$

This equation is important when discussing how to derive the total cross-section given the differential cross-section $\frac{\mathrm{d}^2\sigma}{\mathrm{d}x\,\mathrm{d}y}$.

IV. NEUTRINO DEEP INELASTIC SCATTERING

The understanding of DIS is better than SIS or quasi-elastic (QE) scattering because of the asymptotic freedom. At lower energy, the interaction of the $SU(3)$ strong force becomes strong enough that the perturbation theory can not work well. In DIS, the quarks are seen by the incident lepton (neutrinos will be emphasized later in this section) because the energy of neutrinos is high enough.

A. Quark-parton model and structure functions

Based on the kinematics variables defined in Sec. III, the expression of the elastic electron-nucleon scattering cross-section Rosenbluth formula Eq. 20 can also be used for inelastic scattering.

$$\frac{\mathrm{d}\sigma}{\mathrm{d}Q^2} = \frac{4\pi\alpha^2}{Q^4}\left[\frac{G_E^2+\tau G_M^2}{1+\tau}\left(1-y-\frac{m_p^2y^2}{Q^2}\right)+\frac{1}{2}y^2G_M^2\right] \tag{46}$$

$$\frac{\mathrm{d}\sigma}{\mathrm{d}Q^2} = \frac{4\pi\alpha^2}{Q^4}\left[\left(1-y-\frac{m_p^2y^2}{Q^2}\right)f_2(Q^2)+\frac{1}{2}y^2f_1(Q^2)\right] \tag{47}$$

As shown in Eq. 47, the terms related to scattering angles can be absorbed into x and y after changing the variable from Ω to Q^2. In Eq. 47, the G_E and G_M are absorbed into variables $f_1(Q^2)$ and $f_2(Q^2)$. These two variables are only valid to be used in elastic scattering because G_E and G_M do not depend on the potential change of the rest mass of the final states. To generalize the expression for inelastic scattering, where the differential cross section has to be expressed in terms of two independent kinematic quantities, the x "inelasticity" dependence has to be accounted for. Thus, the differential cross-section is rewritten as

$$\begin{aligned}\frac{\mathrm{d}^2\sigma}{\mathrm{d}x\,\mathrm{d}Q^2} =& \frac{4\pi\alpha^2}{Q^4}\left[\left(1-y-\frac{m_p^2y^2}{Q^2}\right)\frac{F_2(x,Q^2)}{x}\right. \\ &\left.+y^2F_1(x,Q^2)\right],\end{aligned} \tag{48}$$

Where the function $f_1(Q^2)$ and $f_2(Q^2)$ have been replaced by two structure functions $F_1(x,Q^2)$ and $F_2(x,Q^2)$. It is impossible to interpret them as the Fourier transform of the charge or magnetic momentum of a proton.

After the systematic study of the structure functions at the Stanford Linear Accelerator Center (SLAC), two important observations were made [17]. The first observation is *Bjorken scaling*, that both F_1 and F_2 are (almost) independent of Q^2, allowing the structure function to be written as

$$F_1(x,Q^2) \approx F_1(x) \tag{49}$$

$$F_2(x,Q^2) \approx F_2(x). \tag{50}$$

The second is the *Callan–Gross relation*, that for Q^2 about $\mathcal{O}(\mathrm{GeV}^2)$, the structure functions F_1 and F_2 are dependent

$$F_2(x) = 2xF_1(x). \tag{51}$$

These experimental results can be understood by the quark-parton model. In the quark–parton model, the basic interaction in deep inelastic electron-proton scattering is elastic scattering from a spin-half quark within the proton. As a high-momentum transfer approximation, any component of the momentum of the struck quark transverse to the direction of motion of the proton is neglected. Hence, in the infinite momentum frame, the four-momentum of the struck quark can be written as

$$p_q = \xi p_2 = (\xi E_2, 0, 0, \xi E_2), \tag{52}$$

where ξ is the fraction of the momentum of the proton carried by the quark. With the relation $\xi^2p_2^2 = m_q^2$, it can be easily shown that $q^2 + 2\xi p_2\cdot q = 0$. So the momentum fraction ξ can be identified as

$$\xi = \frac{-q^2}{2p_2\cdot q} = \frac{Q^2}{2p_2\cdot q} \equiv x. \tag{53}$$

Immediately for the quark, the y_q kinematic variable is equal to that of the nucleon as

$$y_q = \frac{p_q\cdot q}{p_q\cdot p_1} = \frac{xp_2\cdot q}{xp_2\cdot p_1} = y. \tag{54}$$

Given that when electron and quark masses are neglected, the differential cross-section for electron-quark scattering can be expressed as

$$\frac{\mathrm{d}\sigma}{\mathrm{d}q^2} = \frac{2\pi\alpha^2Q_q^2}{q^4}\left[1+\left(1+\frac{q^2}{s}\right)^2\right], \tag{55}$$

the differential cross-section of the electron–nucleon cross-section can be rewritten as

$$\frac{\mathrm{d}^2\sigma}{\mathrm{d}Q^2} = \frac{4\pi\alpha^2Q_q^2}{Q^4}\left[(1-y)+\frac{y^2}{2}\right], \tag{56}$$

which is a direct result of the parton-quark model.

The parton distribution functions (PDFs) have to be introduced to derive the structure function. The PDFs describe the fractional momenta distribution of quarks within the nucleon. The up-quark PDF for the proton is $u^P(x)$. The electron-nucleon DIS can be derived from PDF and a differential cross-section of electron-quark scattering again. The cross-section for elastic scattering from a particular flavor of quark i with charge Q_i in the range $x \to x+\delta x$ is

$$\frac{\mathrm{d}^2\sigma}{\mathrm{d}Q^2} = \frac{4\pi\alpha^2}{Q^4}\left[(1-y)+\frac{y^2}{2}\right]\times Q_i^2q_i^p(x)\delta x, \tag{57}$$

where $q_i^p(x)$ is the PDF for that flavor of quark. Thus, the double differential cross-section can be obtained as

$$\frac{\mathrm{d}^2\sigma^{ep}}{\mathrm{d}x\,\mathrm{d}Q^2} = \frac{4\pi\alpha^2}{Q^4}\left[(1-y)+\frac{y^2}{2}\right]\sum_i Q_i^2q_i^p(x). \tag{58}$$

Comparing this function with Eq. 47,

$$F_2(x,Q^2) = 2xF_1(x,Q^2) = x\sum_i Q_i^2 q_i^p(x). \tag{59}$$

Note the F_1 and F_2 in Eq. 59 have no dependence on Q^2. The quark-parton model naturally predicted Bjorken scaling because of the elastic process between the lepton and the quark.

Additionally, to allow parity violation [18] and account for the difference of strange- and charm-quark sea [19], the neutrino DIS differential cross-section is

$$\begin{aligned}\frac{\mathrm{d}^2\sigma^{\nu p}}{\mathrm{d}x\,\mathrm{d}y} =& \frac{G_F^2 s}{2\pi}\left[(1-y)F_2^{\nu p}(x,Q^2) + y^2 x F_1^{\nu p}(x,Q^2)\right.\\ &\left. + y\left(1-\frac{y}{2}\right)xF_3^{\nu p}(x,Q^2)\right]\\ \frac{\mathrm{d}^2\sigma^{\bar\nu p}}{\mathrm{d}x\,\mathrm{d}y} =& \frac{G_F^2 s}{2\pi}\left[(1-y)F_2^{\bar\nu p}(x,Q^2) + y^2 x F_1^{\bar\nu p}(x,Q^2)\right.\\ &\left. - y\left(1-\frac{y}{2}\right)xF_3^{\bar\nu p}(x,Q^2)\right],\end{aligned} \tag{60}$$

after changing the variable of interest to from (x,Q^2) to (x,y).

Using a customized parameterization (the detailed definition of $Y_\pm$ will be introduced in Sec. IV B),

$$\begin{aligned}\sigma_{r,\mathrm{NC}}^{\pm} &= \frac{\mathrm{d}^2\sigma_{\mathrm{NC}}^{e^\pm p}}{\mathrm{d}x\,\mathrm{d}Q}\frac{Q^4 x}{2\pi\alpha^2 Y_+}\\ &= F_2 \mp \frac{Y_-}{Y_+}xF_3 - \frac{y^2}{Y_+}F_L,\end{aligned} \tag{61}$$

HERA [13] experiment provided direct measurements and combined cross-section and structure functions analysis of a wide energy range of $e^\pm p \to e^\pm X$ scattering.

Fig. 6 shows the inclusive NC cross-section of $e^- p \to e^- X$ in HERA with a mono-energetic electron beam.

B. Factorization of structure functions

But as more experiential accumulates, clear deviations of interactions from the simple quark-parton model are observed. QCD theory shows that to get a first-principle-derived cross-section of DIS, many kinds of corrections are needed, which will not be covered here. Instead, the experiential measurements and extrapolation, and generalization of data are the common approaches when calculating DIS cross-section for neutrino experiments.

Alternative to Eq. 60, the differential cross section is usually expressed [15] as

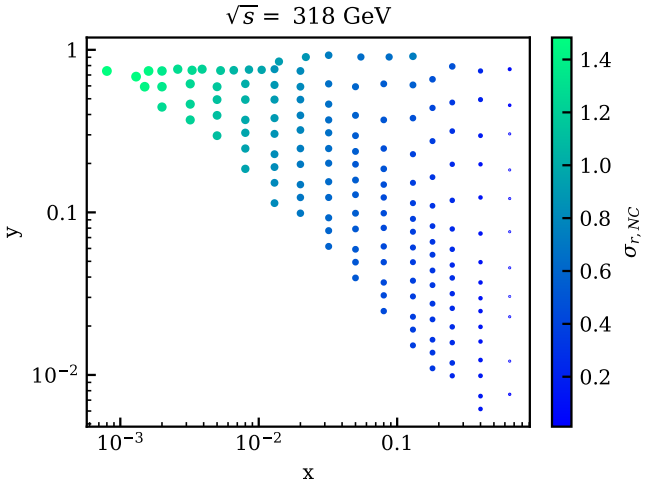

FIG. 6. Inclusive neutral-current (NC) (normalized) cross-section of $e^- p \to e^- X$ in HERA with center-of-mass energy $\sqrt{s}$=318GeV.

$$\begin{aligned}\frac{\mathrm{d}^2\sigma^{\nu A}(x,Q^2,y)}{\mathrm{d}x\,\mathrm{d}y} =& \frac{G_F^2 s/2\pi}{\left(1+Q^2/m_W^2\right)^2}\left[(1-y)F_2^{\nu A}(x,Q^2)\right.\\ &+ y^2 x F_1^{\nu A}(x,Q^2)\\ &\left.+ y\left(1-\frac{y}{2}\right)xF_3^{\nu A}(x,Q^2)\right]\\ =& \frac{G_F^2 s/4\pi}{\left(1+Q^2/m_W^2\right)^2}\left[Y_+F_2^{\nu A}(x,Q^2)\right.\\ &\left.- y^2 F_L^{\nu A}(x,Q^2) + Y_- xF_3^{\nu A}(x,Q^2)\right]\end{aligned} \tag{62}$$

where the $F_1^{\nu A}(x,Q^2)$ is absorbed into the longitudinal structure function $F_L^{\nu A}(x,Q^2) = F_2^{\nu A}(x,Q^2) - 2xF_1^{\nu A}(x,Q^2)$, motivate by Callan–Gross relation. $Y_\pm$ is defined as $Y_\pm = 1 \pm (1-y)^2$ for convenience and A denotes the scattered nucleus initially at rest.

Also, the antineutrino-nucleus scattering cross-section is

$$\begin{aligned}\frac{\mathrm{d}^2\sigma^{\bar\nu A}(x,Q^2,y)}{\mathrm{d}x\,\mathrm{d}y} =& \frac{G_F^2 s/2\pi}{\left(1+Q^2/m_W^2\right)^2}\left[(1-y)F_2^{\bar\nu A}(x,Q^2)\right.\\ &+ y^2 x F_1^{\bar\nu A}(x,Q^2)\\ &\left.+ y\left(1-\frac{y}{2}\right)xF_3^{\bar\nu A}(x,Q^2)\right]\\ =& \frac{G_F^2 s/4\pi}{\left(1+Q^2/m_W^2\right)^2}\left[Y_+F_2^{\bar\nu A}(x,Q^2)\right.\\ &\left.- y^2 F_L^{\bar\nu A}(x,Q^2) - Y_- xF_3^{\bar\nu A}(x,Q^2)\right].\end{aligned} \tag{63}$$

There is no standard widely accepted procedure for the determination of F_2, F_L, xF_3. In the work done for

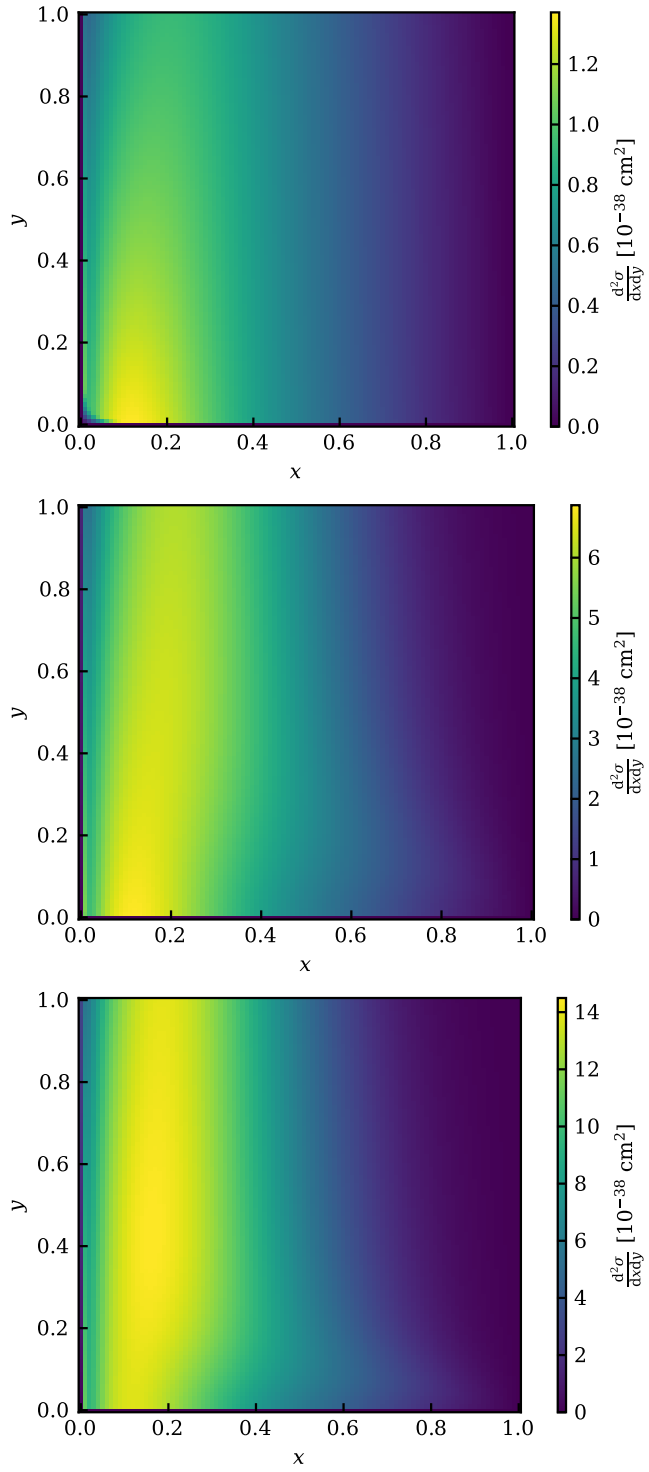

FIG. 7. From top to bottom are the differential cross section $\frac{d^2\sigma}{dx\,dy}$ of 1GeV, 5GeV, and 10GeV ν_μ neutrino with one nucleon in ^{39}Ar.

describing the neutrino structure function for the state-of-the-art widest range of energy [15], the factorization of structure functions is defined as

$$F_i^{\nu A}(x,Q^2) = \sum_{j=q,\bar{q},g} \int_x^1 \frac{\mathrm{d}z}{z} C_{i,j}^{\nu N}\left(z,\alpha_s(Q^2)\right) f_j^{(A)}\left(\frac{x}{z},Q^2\right) \tag{64}$$

$$C_{i,j}^{\nu N}\left(z,\alpha_s(Q^2)\right) = \sum_{k=0}^{m} \left(\alpha_s(Q^2)\right)^k C_{i,j}^{\nu N(k)}(z), \tag{65}$$

where $C_{i,j}^{\nu N}$ is process-dependent and target-independent coefficient function; $f_j^{(A)}$ is target-dependent, indicating the PDFs of the average nucleon bound into a nucleus with mass number A. The work was based on YADISM [20], which provides the perturbative QCD calculation. The coefficient functions are fitted with the unbiased neural networks with experiential data as inputs. The structure functions as the output are saved the fitted functions in the popular format as LHAPDF [21] with replicas indicating the uncertainties and are already made compatible with popular neutrino event generators like GENIE [22]. In Sec. V, these structure functions are used for evaluating the systematic uncertainties of DIS cross-section and their impact on oscillation parameters determination.

Fig. 7 shows the differential cross-section of the neutrino with various energies. When the energy of neutrinos increases, the distribution tends to move to lower x and higher y, indicating the stronger inelastic nature of the scattering.

By integrating the two dimensionless variables x and y in $(0,1)\times(0,1)$ panel, the cross section and its uncertainty can be calculated in Fig. 8.

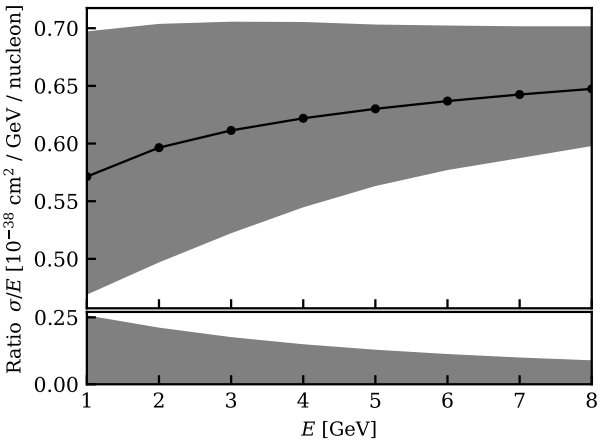

FIG. 8. DIS inclusive cross-section of various neutrino energies from [15]. The band shows the $\pm\sigma$ quantiles of cross-section using the replicas of the structure function provided. The bottom panel shows the relative uncertainty of the cross-section for different energies. The uncertainty is higher for lower energy because the perturbative calculation is more invalid in lower energy.

Later, these uncertainties are applied when constraining the oscillation parameters θ_{23} and δ_{cp}.

V. IMPLICATION FOR FUTURE NEUTRINO OSCILLATION EXPERIMENTS

In this section, a simplified $\mathcal{O}$(GeV) accelerator neutrino experiment to determine the oscillation parameters θ_{23} and δ_{cp} is proposed, and the rate of targeted events is predicted with the Deep Underground Neutrino Experiment (DUNE) conceptual design report [16]. The codes used for the sensitivity projection are for public access [23].

Given a pure $\mathcal{O}$(GeV) ν_μ collimated source aiming at the Earth, the appearance probability of ν_e which can be detected by DIS is [24]

$$\begin{aligned} P(\nu_\mu \to \nu_e) \simeq & \sin^2\theta_{23}\sin^2 2\theta_{13}\frac{\sin^2(\Delta_{31}-aL)}{(\Delta_{31}-aL)^2}\Delta_{31}^2 \\ & + \sin 2\theta_{23}\sin 2\theta_{13}\sin 2\theta_{12}\frac{\sin(\Delta_{31}-aL)}{(\Delta_{31}-aL)} \\ & \cdot \Delta_{31}\frac{\sin(aL)}{(aL)}\Delta_{21}\cos(\Delta_{31}+\delta_{CP}) \\ & + \cos^2\theta_{23}\sin^2 2\theta_{12}\frac{\sin^2(aL)}{(aL)^2}\Delta_{21}^2, \end{aligned} \tag{66}$$

where $\Delta_{ij} = \Delta m_{ij}^2 L/4E_\nu$ and $a = G_F N_e/\sqrt{2}$. For the detector located about L=1300km from the accelerator and proton target, such as DUNE, using the best-fit normal hierarchy (NH) neutrino masses from NuFIT 6.0 [25], the appearance probability can be calculated.

From Fig. 9, the Δm_{23}^2 influence the oscillation phase of the $\mathcal{O}$(GeV) neutrino, while $\sin^2\theta_{23}$ and $\delta_{\rm CP}$ have impact on the rate of ν_e DIS that can be observed.

A. A simplified of LAr long-baseline neutrino experiments

To show the impacting factors clearly, some simplifications of the DUNE experiment will be applied and justified:

- There will be no background of ν_e or $\bar{\nu}_e$ in beam as simplification.
- Because the cross-section of DIS of anti-neutrino is less than that of neutrino by a factor of about 3, shown in Sec. II B and Ref. [15], only the neutrino-beam mode is assumed from the neutrino source.
- Only charge current interaction via the W boson is assumed because particle identification is needed in the following procedure.

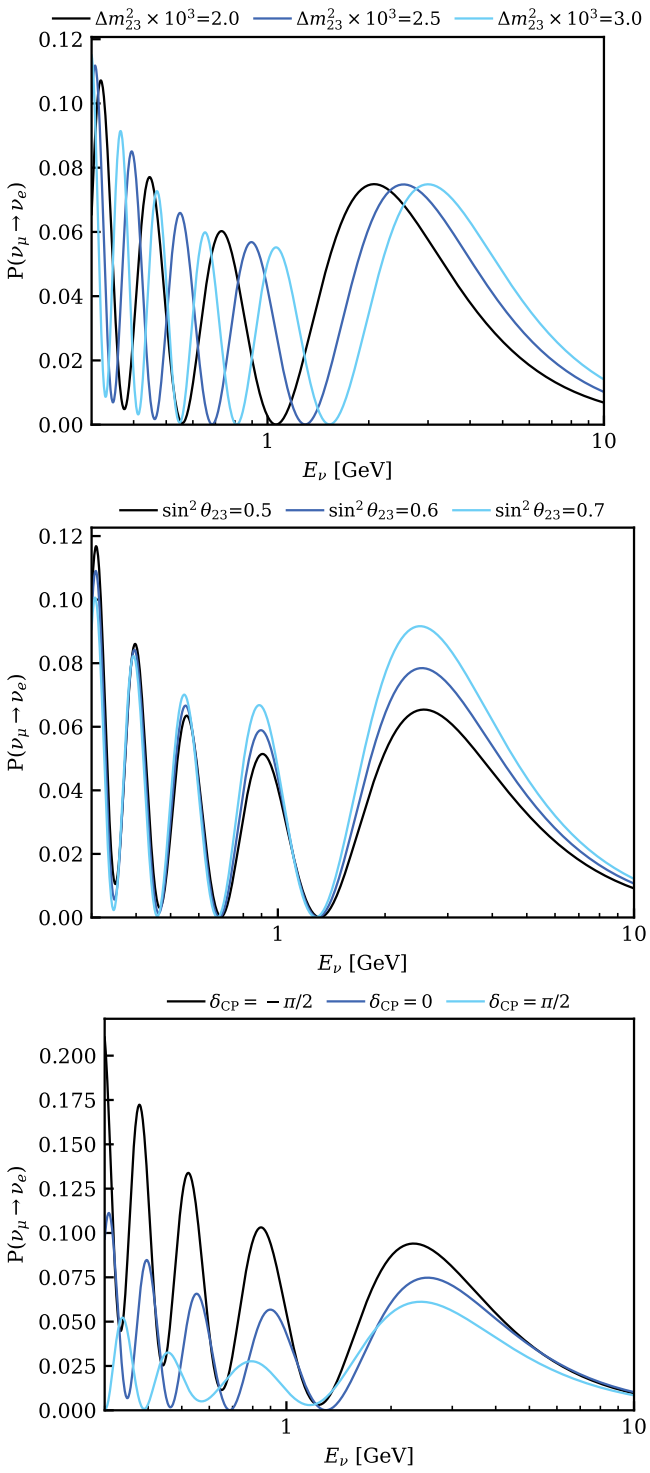

FIG. 9. Appearance probability for a range of neutrino energy when oscillation parameters are taken as NuFIT 6.0 best-fit except Δm_{23}^2, $\sin^2\theta_{23}$, and $\delta_{\rm CP}$ from top to bottom indicted in above the plot.

- Only DIS is assumed to happen and got detected with detection efficiency 100% to remove the influence of other interaction channels, such as QE.

- The DIS of ν_ν and ν_e produce muon and electron respectively. Here, the perfect particle identification, equivalent to perfect interaction identification, is assumed.
- In principle, the reconstructive energy of the incident neutrino will be deteriorated by the finite energy resolution and detector effects. Here, no smearing of the detected energy spectrum is assumed.
- Though the energy range of neutrinos from the source is wide and the potential statistics of events are high enough to perform an unbinned likelihood construction, here the binned likelihood construction, assuming Gaussian statistics in each bin, is applied. The binning is chosen linearly from 0.5GeV to 8.5GeV, with 8 bins. The bin centers are the integers of energy in the GeV unit.
- The liquid Argon (LAr) detector is assumed to be perfectly uniform in density and response, assuming zero non-uniformity.
- The livetime and LAr sensitive mass of the experiment is assumed to be 3 years and 10^4 tonne.
- The uncertainty of cross-section is assumed to deviate in the same direction (increase and decrease) for different energies to exaggerate the impact of overestimation and underestimation of cross-section, while no shape uncertainty is directly assigned.

B. Uncertainty of ν_e appearance measurement

The near detector neutrino flux is extracted from Fig. 4.10 in Ref. [26] and shown in Fig. 10.

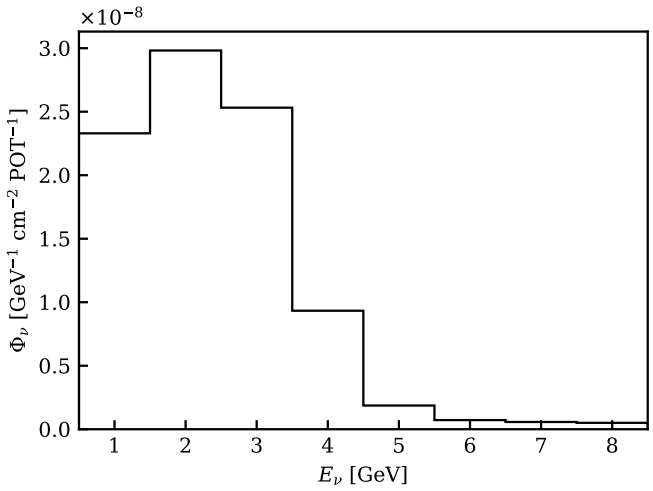

FIG. 10. DUNE near detector ν_μ neutrino flux.

The ν_μ neutrino flux is considerably high, due to the high proton on target (POT) rate 1.1×10^{21} per year, to measure DIS and other channels' neutrino interaction cross-section precisely.

The far-near detector total neutrino flux ratio is extracted from Fig. 4.8 in Ref. [26] and shown in Fig. 11, in preparation for the calculation of neutrino flux in the far detector.

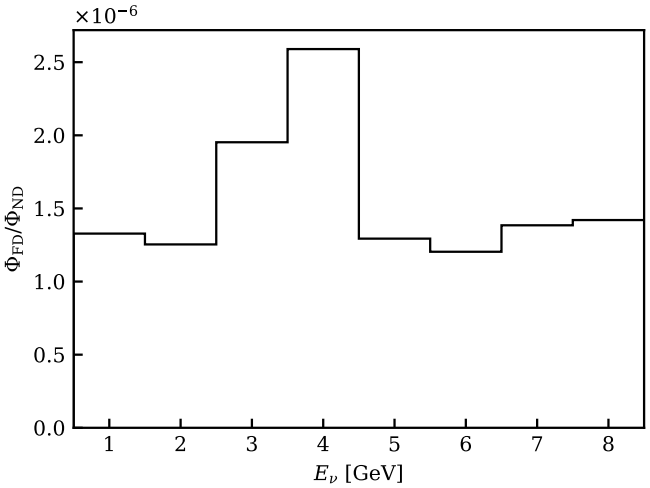

FIG. 11. The far-near detector total neutrino flux ratio.

The non-uniform structure might have originated from the different solid angles of near and far detectors.

Combining the information from Fig. 10 and Fig. 11, the far detector neutrino flux can be calculated and shown in Fig. 12.

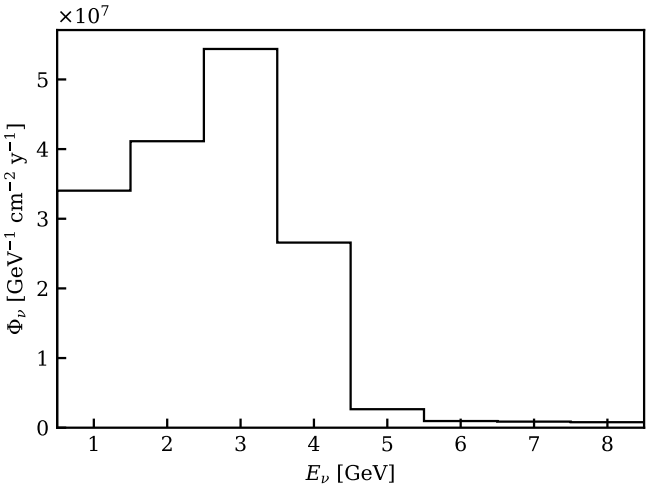

FIG. 12. Far detector inclusive neutrino flux.

Using the best estimation of DIS cross-section in Fig. 8, far detector flux, and number of ^{39}Ar, the DIS event rate is shown in Fig. 13.

The uncertainty due to the uncertainty from the DIS cross section is shown in the black band.

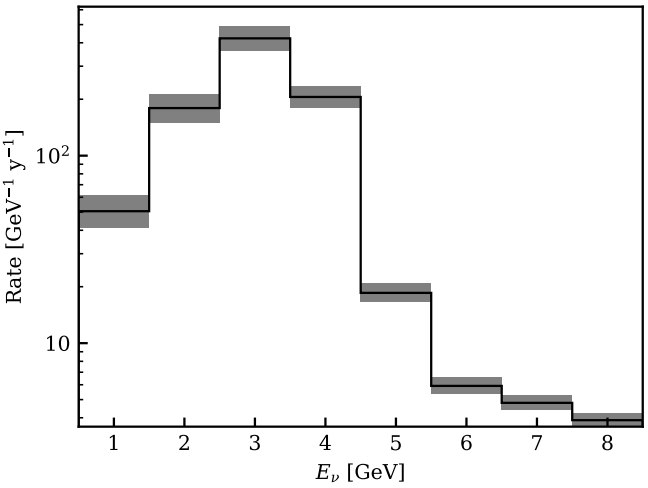

FIG. 13. ν_e DIS events rate and its uncertainty in the far detector per year.

C. Impact on θ_{23} and δ_{cp} sensitivity

The expected number of observed events in the far detector in the defined livetime is proportional to the histogram in Fig. 13. For one trial of measurement, the likelihood in Eq. 67 can be defined to show how the parameter set $(\Delta m^2, \theta)$ is allowed by the observation.

$$\chi^2 = \sum_i \left[\frac{\left(N_{\text{obs},i} - N_{\text{exp},i}(t, \Delta m^2, \theta)\right)^2}{\sigma^2_{\text{stat},i}} \right] + t^2 \tag{67}$$

The index i goes through the bins. The N_{obs} is the observation of the experiment while assuming the true oscillation parameters are the best-fit of NuFIT 6.0 [25] except δ_{CP}, which is assumed to be 0. N_{exp} is a function of oscillation parameters and t, which is the parameter following a Gaussian distribution and mapped to the corresponding quantile of the distribution of cross-section in Fig. 8.

In this section, the true oscillation parameters are assumed as the best fit of NuFIT 6.0 [25] and $\delta_{cp} = 0$. Other parameters are fixed in the fitting except θ_{23} (δ_{cp}) and t, which is equivalent to assuming uncertainties of other parameters are lower enough than the statistics of events. By scanning through the mathematically allowed range of $\sin^2\theta_{23}$ (δ_{cp}), the $\Delta\chi^2$ curves under different fractions of uncertainty of DIS cross-section are shown in Fig. 14.

If the systematic uncertainty of the DIS cross-section can be 0, the improvement of $\sin^2\theta_{23}$ (δ_{cp}) is a factor of about 3 reduction of the resolution. This reduction will be changed if we assume a different detector configuration obviously, but can already show the large impact of systematic uncertainty of DIS cross-section.

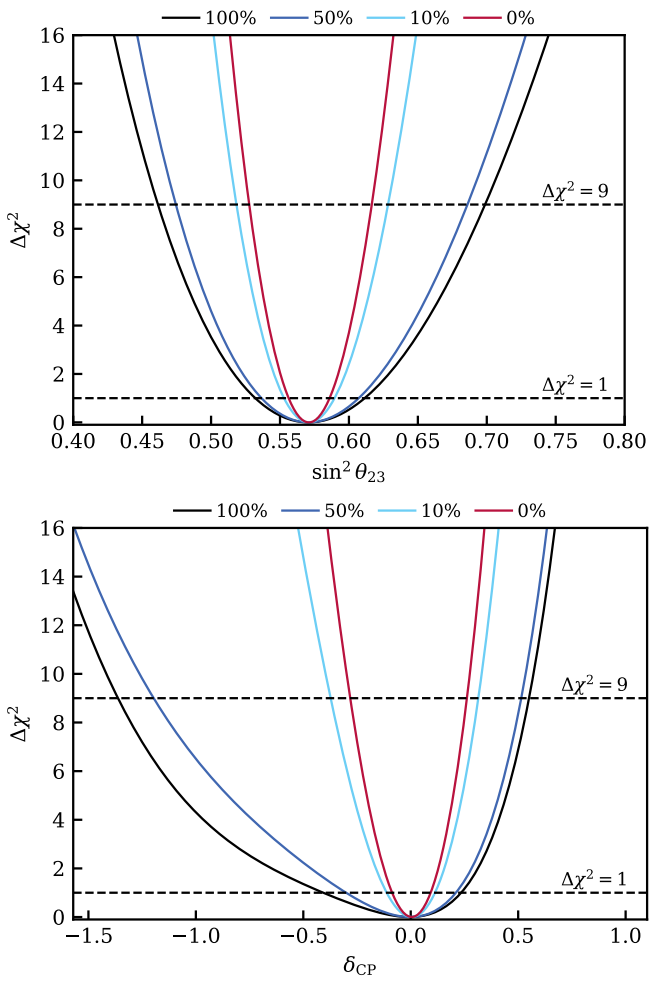

FIG. 14. The expected constraint on $\sin^2\theta_{23}$ and δ_{cp} under different assumptions of the size of systematic uncertainty of DIS. The two horizontal lines show the $\Delta\chi^2 = 1, 9$, indicating ±1 and ±3 σ constraint in the asymptotic approach of likelihood assuming its χ^2 distribution.

The two-dimensional 3σ constraint can also be obtained while allowing $(\sin^2\theta_{23}, \delta_{cp})$ and t changing in the optimization of best-fit likelihood. The 3σ contour of $(\sin^2\theta_{23}, \delta_{cp})$ is shown in Fig. 15.

In Fig. 14 and Fig. 15, the constraint indicated with zero systematic uncertainty is the statistical uncertainty from the limited number of events in the (simplified) experiment.

VI. CONCLUSION

The cross-sections of $\mathcal{O}$(GeV) neutrino and nucleus interactions have been derived, along with their associated uncertainties as reported in the literature. It is evident that the theoretical uncertainties in deep inelastic scattering (DIS) for $\mathcal{O}$(GeV) neutrinos currently exceed the potential statistical uncertainties anticipated in near-

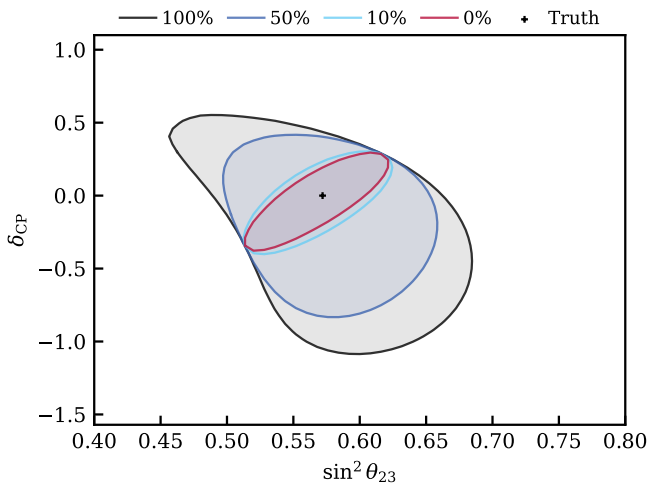

FIG. 15. The two-dimensional 3σ constraint of $(\sin^2\theta_{23}, \delta_{cp})$ under different assumptions of the size of systematic uncertainty of DIS.

future long-baseline experiments. This underscores the necessity of a near-far detector configuration to achieve the precision required for measuring key oscillation parameters, such as θ_{23} and δ_{cp}, thereby improving their resolution.

Moreover, the significant uncertainty in DIS cross-sections also affects atmospheric neutrinos, whose energies lie in a range where perturbative QCD is inapplicable. Future experimental measurements of neutrino interactions can provide critical data to refine theoretical models of DIS cross-sections, ultimately benefiting both atmospheric and accelerator-based neutrino physics.

VII. READING MATERIALS

Ref. [7, 10, 15, 27–31], Sec. 18 (Structure Functions), Sec. 19 (Fragmentation Functions in e^+e^-, ep, and (pp) Collisions) of [32], and Chpt. 8 (Deep inelastic scattering), and Chpt. 12 (The weak interactions of leptons, especially the Sec. 12.2 (Neutrino scattering)) of [18].

[1] C. L. Cowan, F. Reines, F. B. Harrison, H. W. Kruse, and A. D. McGuire, Detection of the free neutrino: A Confirmation, Science **124**, 103 (1956).

[2] K. Hirata *et al.* (Kamiokande-II), Observation of a Neutrino Burst from the Supernova SN 1987a, Phys. Rev. Lett. **58**, 1490 (1987).

[3] R. Davis, Jr., D. S. Harmer, and K. C. Hoffman, Search for neutrinos from the sun, Phys. Rev. Lett. **20**, 1205 (1968).

[4] Q. R. Ahmad *et al.* (SNO), Measurement of the rate of $\nu_e + d \to p + p + e^-$ interactions produced by ^{8}B solar neutrinos at the Sudbury Neutrino Observatory, Phys. Rev. Lett. **87**, 071301 (2001), arXiv:nucl-ex/0106015.

[5] Y. Fukuda *et al.* (Super-Kamiokande), Evidence for oscillation of atmospheric neutrinos, Phys. Rev. Lett. **81**, 1562 (1998), arXiv:hep-ex/9807003.

[6] K. Eguchi *et al.* (KamLAND), First results from KamLAND: Evidence for reactor anti-neutrino disappearance, Phys. Rev. Lett. **90**, 021802 (2003), arXiv:hep-ex/0212021.

[7] K. Abe *et al.* (T2K), Indication of Electron Neutrino Appearance from an Accelerator-produced Off-axis Muon Neutrino Beam, Phys. Rev. Lett. **107**, 041801 (2011), arXiv:1106.2822 [hep-ex].

[8] F. P. An *et al.* (Daya Bay), Observation of electron-antineutrino disappearance at Daya Bay, Phys. Rev. Lett. **108**, 171803 (2012), arXiv:1203.1669 [hep-ex].

[9] M. A. Acero *et al.* (NOvA), First Measurement of Neutrino Oscillation Parameters using Neutrinos and Antineutrinos by NOvA, Phys. Rev. Lett. **123**, 151803 (2019), arXiv:1906.04907 [hep-ex].

[10] J. A. Formaggio and G. P. Zeller, From eV to EeV: Neutrino Cross Sections Across Energy Scales, Rev. Mod. Phys. **84**, 1307 (2012), arXiv:1305.7513 [hep-ex].

[11] P. Vogel and J. F. Beacom, Angular distribution of neutron inverse beta decay, anti-neutrino(e) + p —> e+ + n, Phys. Rev. D **60**, 053003 (1999), arXiv:hep-ph/9903554.

[12] F. D. Aaron *et al.* (H1, ZEUS), Combined Measurement and QCD Analysis of the Inclusive e+- p Scattering Cross Sections at HERA, JHEP **01**, 109, arXiv:0911.0884 [hep-ex].

[13] H. Abramowicz *et al.* (H1, ZEUS), Combination of measurements of inclusive deep inelastic $e^{\pm}p$ scattering cross sections and QCD analysis of HERA data, Eur. Phys. J. C **75**, 580 (2015), arXiv:1506.06042 [hep-ex].

[14] A. Bodek and U. K. Yang, Modeling deep inelastic cross-sections in the few GeV region, Nucl. Phys. B Proc. Suppl. **112**, 70 (2002), arXiv:hep-ex/0203009.

[15] A. Candido, A. Garcia, G. Magni, T. Rabemananjara, J. Rojo, and R. Stegeman, Neutrino Structure Functions from GeV to EeV Energies, JHEP **05**, 149, arXiv:2302.08527 [hep-ph].

[16] B. Abi *et al.* (DUNE), Deep Underground Neutrino Experiment (DUNE), Far Detector Technical Design Report, Volume I Introduction to DUNE, JINST **15** (08), T08008, arXiv:2002.02967 [physics.ins-det].

[17] J. I. Friedman and H. W. Kendall, Deep inelastic electron scattering, Ann. Rev. Nucl. Part. Sci. **22**, 203 (1972).

[18] M. Thomson, *Modern Particle Physics* (Cambridge University Press, 2013).

[19] G. Onengut *et al.* (CHORUS), Measurement of nucleon structure functions in neutrino scattering, Phys. Lett. B **632**, 65 (2006).

[20] A. Candido, F. Hekhorn, G. Magni, T. R. Rabemananjara, and R. Stegeman, Yadism: yet another deep-inelastic scattering module, Eur. Phys. J. C **84**, 698 (2024), arXiv:2401.15187 [hep-ph].

[21] A. Buckley, J. Ferrando, S. Lloyd, K. Nordström, B. Page, M. Rüfenacht, M. Schönherr, and G. Watt, LHAPDF6: parton density access in the LHC precision era, Eur. Phys. J. C **75**, 132 (2015), arXiv:1412.7420 [hep-ph].

[22] C. Andreopoulos *et al.*, The GENIE Neutrino Monte Carlo Generator, Nucl. Instrum. Meth. A **614**, 87 (2010), arXiv:0905.2517 [hep-ph].
[23] https://github.com/dachengx/fitdis.
[24] H. Nunokawa, S. J. Parke, and J. W. F. Valle, CP Violation and Neutrino Oscillations, Prog. Part. Nucl. Phys. **60**, 338 (2008), arXiv:0710.0554 [hep-ph].
[25] I. Esteban, M. C. Gonzalez-Garcia, M. Maltoni, I. Martinez-Soler, J. a. P. Pinheiro, and T. Schwetz, NuFit-6.0: Updated global analysis of three-flavor neutrino oscillations, (2024), arXiv:2410.05380 [hep-ph].
[26] B. Abi *et al.* (DUNE), Deep Underground Neutrino Experiment (DUNE), Far Detector Technical Design Report, Volume II: DUNE Physics, (2020), arXiv:2002.03005 [hep-ex].
[27] P. Lipari, M. Lusignoli, and F. Sartogo, The Neutrino cross-section and upward going muons, Phys. Rev. Lett. **74**, 4384 (1995), arXiv:hep-ph/9411341.
[28] G. P. Zeller *et al.* (NuTeV), A Precise Determination of Electroweak Parameters in Neutrino Nucleon Scattering, Phys. Rev. Lett. **88**, 091802 (2002), [Erratum: Phys.Rev.Lett. 90, 239902 (2003)], arXiv:hep-ex/0110059.
[29] K. Xie, J. Gao, T. J. Hobbs, D. R. Stump, and C. P. Yuan (CTEQ-TEA), High-energy neutrino deep inelastic scattering cross sections, Phys. Rev. D **109**, 113001 (2024), arXiv:2303.13607 [hep-ph].
[30] A. A. Aguilar-Arevalo *et al.* (MiniBooNE), First Measurement of the Muon Neutrino Charged Current Quasielastic Double Differential Cross Section, Phys. Rev. D **81**, 092005 (2010), arXiv:1002.2680 [hep-ex].
[31] S. Abe *et al.* (KamLAND), First measurement of the strange axial coupling constant using neutral-current quasielastic interactions of atmospheric neutrinos at KamLAND, Phys. Rev. D **107**, 072006 (2023), arXiv:2211.13911 [hep-ex].
[32] S. Navas *et al.* (Particle Data Group), Review of particle physics, Phys. Rev. D **110**, 030001 (2024).